



HAL
open science

Vegetal-extracted polyphenols as a natural hard carbon anode source for Na-ion batteries

Adrian Beda, Angel Escamilla Pérez, Loic Simonin, Camelia Matei Ghimbeu

► **To cite this version:**

Adrian Beda, Angel Escamilla Pérez, Loic Simonin, Camelia Matei Ghimbeu. Vegetal-extracted polyphenols as a natural hard carbon anode source for Na-ion batteries. *ACS Applied Energy Materials*, 2022, 5 (4), pp.4774-4787. 10.1021/acsaem.2c00215 . cea-03713194

HAL Id: cea-03713194

<https://cea.hal.science/cea-03713194>

Submitted on 22 Nov 2023

HAL is a multi-disciplinary open access archive for the deposit and dissemination of scientific research documents, whether they are published or not. The documents may come from teaching and research institutions in France or abroad, or from public or private research centers.

L'archive ouverte pluridisciplinaire **HAL**, est destinée au dépôt et à la diffusion de documents scientifiques de niveau recherche, publiés ou non, émanant des établissements d'enseignement et de recherche français ou étrangers, des laboratoires publics ou privés.

Vegetal-extracted polyphenols as a natural hard carbon anode source for Na-ion batteries

Adrian Beda^{a,b}, Angel M. Escamilla-Pérez^a, Loïc Simonin^c, Camélia Matei Ghimbeu^{a,b,d,}*

^a Université de Haute-Alsace, Institut de Science des Matériaux de Mulhouse (IS2M), CNRS,
UMR 7361, F-68100 Mulhouse, France

^b Université de Strasbourg, F-67081 Strasbourg, France

^c Université Grenoble Alpes, CEA, LITEN, DEHT, LM 17 rue des Martyrs, 38054 Grenoble
cedex 9, France

^d Réseau sur le Stockage Electrochimique de l'Energie (RS2E), HUB de l'Energie, FR CNRS
3459, 80039 Amiens, France

* E-mail: camelia.ghimbeu@uha.fr

Abstract

Hard carbons are promising anode materials for Na-ion batteries that can be produced using a wide variety of synthetic or natural precursors. This work focuses on the development of hard carbons from natural polyphenols derived from different vegetal extracts. Herein, five natural tannin-based polyphenols (catechu, chestnut, myrobalan and two mimosa extracts) were used to synthesize hard carbons after a single pyrolysis process at 1500 °C. The morphology, texture, structure and surface chemistry of these materials were characterized. The precursors lead to a high carbon yield of 35-44%, and the obtained hard carbons have disordered structures. N₂ and CO₂ physisorption assays revealed the presence of a low volume of meso-, micro- and ultra-micropores and very low specific surface areas (SSAs) (N₂-SSA < 7 m²·g⁻¹ and CO₂-SSA < 24 m²·g⁻¹). These materials exhibit a typical hard carbon structure with large interlayer spacing (d₀₀₂ between 3.55 Å and 3.67 Å) and a small amount of inorganic compounds (< 6 wt.%). The electrochemical performance showed a high initial Coulombic efficiency (iCE > 84%), which reached 100% after a few cycles, as well as good cycling stability. Myrobalan- and mimosa-based hard carbons exhibited reversible capacities of approximately 304 mAh·g⁻¹ when cycled at C/10 (C=372 mA·g⁻¹), whereas catechu- and chestnut-derived hard carbons exhibited reversible capacities of 280 mAh·g⁻¹, due to the presence of impurities, localized graphitic domains and slightly lower d₀₀₂ values. In addition, the electrochemical behaviour of myrobalan- and mimosa-based hard carbons is stable at higher current densities (C), while the capacity decreases for the other materials. The best performance was achieved for materials with low impurity levels, more disordered structures and low specific surface areas (*i.e.*, myrobalan-derived hard carbon).

Keywords: Hard carbon; Na-ion battery; natural polyphenols; tannins; vegetal extracts; Ar pyrolysis

1. Introduction

Energy storage demand has increased in recent years, and this trend is likely to continue given the global transition from fossil fuels towards renewable energy resources.^{1,2} However, the variability of the latter requires the implementation of enhanced energy storage devices, which are critical for maximizing the benefits of those resources. Indeed, it is of utmost importance to store the energy generated by renewable resources to deliver it when needed. Li-ion batteries (LIBs) currently dominate the energy storage market, and despite the fact that LIBs have been widely commercialized since the early 1990s,³ their utilization for large-scale energy storage has been delayed due to safety issues, high production costs and the limited and uneven distribution of lithium resources around the world.⁴ These are the principal reasons why researchers are looking for a safer, lower-cost and greener energy storage technology. One attractive alternative to Li-ion batteries is Na-ion batteries (SIBs). Because sodium and lithium have similar physical and chemical properties, sodium has attracted interest as a lithium substitute in secondary batteries; in addition, sodium is more abundant and less expensive than lithium.⁵ Furthermore, unlike LIBs, SIB anode current collectors can be processed with aluminium instead of copper, lowering manufacturing costs for SIBs.⁶

However, the main drawback that limits the widespread commercialization of SIBs is the electrode materials, particularly on the anode side. Efforts have been made to develop active materials that can perform stably and deliver high capacity cycling performance over a longer lifetime. Layered oxides and phosphates,⁷⁻⁹ polyanionic compounds^{10,11} and Prussian blue analogues¹² with good electrochemical properties have been developed as SIB cathode materials, whereas carbon-based materials have dominated anode research. Graphite, the most commonly used anode material for LIBs, showed poor Na⁺ ion intercalation at an early stage. Indeed, graphite intercalation compounds (GICs) with sodium are thermodynamically unstable¹³⁻¹⁵, and graphite can only cointercalate solvated Na ions.^{16,17} Thus, research has

focused on other carbonaceous materials, such as soft carbons (SCs), hard carbons (HCs) and heteroatom-rich carbons, as potential economical anode materials.^{2,18–21} Among these options, hard carbons are the most promising anode material for SIB applications.

Hard carbons, which are non-graphitizable carbon materials, exhibit a disordered-like nature and are composed of turbostratic graphene layers (*i.e.*, pseudo-graphitic domains) arranged randomly with open and close porosity between the domains. This structure, commonly known as the “house of cards”,^{18,22} has been demonstrated to be favourable for sodium storage by adsorption on structural defects, nanopore filling and intercalation into graphene sheets.^{23,24} In fact, hard carbons possess larger interlayer spaces than graphite, making intercalation of larger Na⁺ ions easier (*i.e.*, ionic radii: 1.02 Å for Na⁺ vs. 0.76 Å for Li⁺).²⁵ Regardless, the sodium storage mechanisms are not yet fully understood,^{2,26} and hard carbons generally have a low initial Coulombic efficiency (iCE), mainly due to the formation of a solid electrolyte interface (SEI).²⁷

Many works have successfully reported hard carbons synthesized from a wide variety of precursors for sodium ion storage applications, as reviewed elsewhere.²⁸ This includes waste engineering plastics (*e.g.*, PC/PET,²⁹ PVC³⁰), biomasses (*e.g.*, fruit/vegetable peels,³¹ nut shells,³² plants/trees³³, kelp³⁴), biopolymers (*e.g.*, cellulose,^{35,36} sucrose,³⁷ chitosan³⁸) and phenolic resins.^{6,25,39–42} Hard carbons are primarily synthesized by pyrolysis at temperatures above 900 °C, and their structure is closely related to the precursors used as well as the pyrolysis conditions.⁴³ Furthermore, the presence of other chemical elements, particularly oxygen, boosts the suppression of carbon rearrangements during the pyrolysis step, resulting in turbostratic microstructures.⁴⁴

Despite the abundance and wide variety of biomass precursors, most depend on the season and geography, which might lead to a lack of reproducibility in terms of composition/structure. On the other hand, the precursors used for preparing phenolic resins are expensive and toxic.⁴⁵

For instance, Hasegawa *et al.*⁴⁰ and Asfaw *et al.*³⁹ used resorcinol and formaldehyde to prepare hard carbon monoliths and hard carbon microspheres, respectively. They controlled the material properties by modifying the pyrolysis temperature. The best electrochemical performance was obtained at temperatures ranging from approximately 1500 to 1600 °C, leading to specific capacities ranging from 330 to 350 mAh·g⁻¹. In addition, Hasegawa *et al.*⁴⁰ reached one of the highest iCEs (92%) using a binder/additive-free monolith with a low specific surface area (3.8 m²·g⁻¹). Other authors have favoured the use of carcinogenic phenol instead of resorcinol for resin preparation. Two examples are the preparation of hard carbon microspheres using a hydrothermal carbonization method by Wang *et al.*⁴⁶ and the multistep synthesis process (solution - spray drying - preoxidation) developed by Shi *et al.*⁴⁷ Hard carbon microspheres were obtained at lower pyrolysis temperatures (1250 °C and 1100 °C, respectively), leading to higher initial specific capacities (517 mAh·g⁻¹ and 394 mAh·g⁻¹). However, the high specific surface area of Wang's HC microspheres⁴⁶ drops off the iCE to 60% (*i.e.*, reversible capacity of 300 mAh·g⁻¹), whereas the multistep synthesis⁴⁷ achieves 85% iCE (*i.e.*, reversible capacity of 334 mAh·g⁻¹). It is worth noting that all works detailed above have cycled their materials at a low current density of 20 mA·g⁻¹, which might promote larger capacities. Greener phenolic resin synthesis methods have also been proposed, such as the use of phloroglucinol and glyoxylic acid²⁵ extracted from natural sources. Hard carbons obtained in this manner have been tested as anodes for SIBs, yielding reversible capacities of approximately 270 mAh·g⁻¹ with iCEs of 76% when cycled at a higher current density (37.2 mA·g⁻¹). The main disadvantage of these precursors is their higher cost than other natural resources (price comparison presented in Table S1, Supporting Information). One eco-friendly solution to cost and toxicity issues is to use natural polyphenols as hard carbon precursors. Polyphenols are phenol-based molecules produced by the secondary metabolism of plants.⁴⁸ Tannins, the natural counterpart of resorcinol, belong to this family and are classified into two categories: hydrolysable tannins and

condensed tannins. They are abundant, nontoxic and economical; in addition, they can be extracted from different tree barks at an industrial scale. Indeed, tannins are among the only natural resources with reproducible compositions that can be produced at large scales and used for various carbon production.^{45,49–51} Tannin-based polyphenols were first proposed by our group as green and efficient precursors for hard carbon sphere preparation and utilization as high-performance anodes in SIBs ($\sim 300 \text{ mAh}\cdot\text{g}^{-1}$ at $50 \text{ mA}\cdot\text{g}^{-1}$).⁵² This patented procedure involves the polymerization and precipitation of tannins and a cross-linker, followed by a pyrolysis step. Therefore, a simplified single-step pyrolysis method for synthesizing hard carbon materials from tannins is of great interest. In addition, the high amount of carbon derived from such polyphenols makes them appropriate candidates for use as sole carbon sources.

Motivated by such advantages, this work proposes a green approach for synthesizing hard carbons from natural polyphenols with a single pyrolysis step. This process reduces both cost and time by using less expensive precursors and simplifying the synthesis method. Five different extracts containing either hydrolysable or condensed tannins were selected as precursors. The influence of the carbon source on the resulting HC properties (morphology, structure, texture and composition) was evaluated. These materials were then tested as SIB anodes, exhibiting reversible capacities between 277 and 304 $\text{mAh}\cdot\text{g}^{-1}$ at C/10 and an initial Coulombic efficiency greater than 84%. The differences in material performance are discussed in terms of carbon properties and the applied electrochemical conditions.

2. Experimental section

2.1. Hard carbon synthesis.

Five polyphenols derived from natural sources were selected for hard carbon synthesis: catechu extract (C), chestnut extract (CH), myrobalan extract (M) and two mimosa extracts, one purchased from Green'ing, France (MG) and one graciously provided by Mimosa Extract Company (Pty) Ltd, South Africa (MC). The precursors were used as-received without any

further purification. The raw materials were heat treated at a heat rate of $5\text{ }^{\circ}\text{C}\cdot\text{min}^{-1}$ at $1500\text{ }^{\circ}\text{C}$ under an Ar flux of $15\text{ L}\cdot\text{h}^{-1}$ and kept for 1 h at this temperature; then, the samples cooled down naturally. The selection of pyrolysis temperature was based on our previous studies⁵³ showing the best electrochemical performance for materials pyrolysed between $1400\text{--}1600\text{ }^{\circ}\text{C}$ temperature range. The as-obtained hard carbons were manually ground for better homogeneity, and they were labelled “HC-X” hereafter, where X designates the nature of the extract used for the heat treatment; *e.g.*, HC-MG is the hard carbon associated with the mimosa extract from Green'ing.

2.2. Physico-chemical characterization

The chemical fingerprint of the precursors was analysed using a Bruker Fourier transform infrared spectrometer (model IFS66/S) with an MCT detector in the $4000\text{--}400\text{ cm}^{-1}$ range. The carbon content was determined by the weight loss during thermal pyrolysis. Additionally, thermogravimetric analysis (TGA) was performed with a Mettler-Toledo TGA 851e by heating the natural extracts to $950\text{ }^{\circ}\text{C}$ at a heating rate of $5\text{ }^{\circ}\text{C min}^{-1}$ under a N_2 atmosphere. Further TGA tests were performed on hard carbons under air to quantify the mass of residual inorganic compounds (residual ashes). The hard carbon morphology was observed by scanning electron microscopy (SEM). Micrographs were acquired with an FEI Quanta 400 scanning electron microscope equipped with a high-resolution low-vacuum field emission gun (FEG). This microscope was also equipped with a JED 2300 detector for energy-dispersive X-ray spectroscopy (EDX) analysis. Several EDX acquisitions (3) were performed in large areas, and the average values are presented herein. X-ray diffraction (XRD) patterns were obtained using a Bruker D8 Advanced diffractometer with flat-plate Bragg–Brentano $\theta\text{--}\theta$ geometry equipped with a LynxEye XE-T high resolution energy dispersive 1-D detector ($\text{Cu K}\alpha_{1,2}$). A step size of 0.01° (2θ scale) in the range of 10 to 90° was used for data acquisition. The graphite interlayer space (d_{002}) was determined by applying the Bragg equation using the $(0\ 0\ 2)$ peak, while the

crystallite sizes L_c and L_a were estimated using the Scherrer equation on the (0 0 2) and (1 0 0) peaks, respectively. The Raman spectra were recorded on a LabRAM BX40 (Horiba Jobin-Yvon) spectrometer equipped with a He–Ne excitation source (532 nm wavelength) at room temperature. Several spectra were acquired (mapping), and the average spectrum was used for this work. High-resolution transmission electron microscopy (HRTEM) images were obtained with a high voltage JEOL ARM-200F instrument operating at 200 kV. The hard carbon surface chemical composition and the nature of the functional groups were analysed by X-ray photoelectron spectroscopy (XPS) in the 0–1200 eV range. The spectra were recorded using a VG Scienta SES 2002 spectrometer equipped with a monochromatic X-ray source ($Al\ K\alpha = 1486.6\text{ eV}$) and a G Scienta XM780 monochromator. N_2 and CO_2 physisorption experiments were carried out at $-196\text{ }^\circ\text{C}$ on a Micromeritics ASAP 2420 instrument and at $0\text{ }^\circ\text{C}$ on a Micromeritics ASAP 2020 instrument, respectively. The samples were first out-gassed under vacuum for 12 h at $300\text{ }^\circ\text{C}$ in the degassing port and then for another 2 h in the analysis port to remove any traces of molecules. The equivalent BET specific surface areas were determined from the linear plot in the relative pressure range P/P_0 of 0.05–0.3 for N_2 and 0.01–0.03 for CO_2 . The pore size distribution was obtained from the N_2 and CO_2 adsorption isotherms using two dimensional nonlocal density functional theory (2D-NLDFT) with a heterogeneous surface pore model for the carbon materials carried out by SAIEUS software (Micromeritics). The density measurements were performed on a Micromeritics AccuPyc II 1340 gas pycnometer. The samples had been previously out-gassed under vacuum for 12 h at $300\text{ }^\circ\text{C}$. Helium (He) was used as the displacement medium, and the density was determined after 100 cycles. Based on the gas adsorption data and the He density, the volume ratio percentages of close porosity (R_{CP}) and open porosity (R_{OP}) were determined according to previously developed methodology.^{38,42}

2.3. Electrochemical characterization

Galvanostatic electrochemical characterizations were performed at room temperature on an Arbin Instrument BT2000 battery cycler operated by MITS PRO software using CR2032-type coin cells. The electrodes were composed of the active material (synthesized hard carbon, 90 wt.%), polyvinylidene fluoride (PVDF 5130 from Solvay, 5 wt.%) as a binder and carbon black (Super C65 from IMERYS, 5 wt.%) as a conductive additive. The slurries were stirred in N-methyl-2-pyrrolidone (NMP from Sigma Aldrich) and uniformly tape casted with a 100 μm long doctor blade onto an aluminium current collector (25 μm thick) using an Elcometer 4340 automatic film applicator. The electrodes (diameter: 14 mm) were cut with a disk cutter and then dried under dynamic vacuum at 80 °C for 48 hours in a Büchi® oven. The coin cells were assembled in a glove box under an Ar atmosphere ($\text{O}_2 < 5 \text{ ppm}$, $\text{H}_2\text{O} < 5 \text{ ppm}$) using sodium metal (Sigma Aldrich 99.9% purity) both as a reference and as a counter electrode (*i.e.*, half-cell configuration). Two separators were employed. The electrolyte, provided by TIAMAT-France, was 1 M NaPF_6 in ethylene carbonate and dimethyl carbonate (EC:DMC, 1:1 vol.) with 2% fluoroethylene carbonate (FEC) as an additive, with 150 μL of the electrolyte deposited over. The electrochemical measurements were performed in two stages during the reduction step: first, a galvanostatic stage in the voltage range of 2.5–0.01 V *vs.* Na^+/Na , followed by a potentiostatic stage at 0.01 V *vs.* Na^+/Na , until the current density reached 3.72 $\text{mA}\cdot\text{g}^{-1}$. The oxidation step was only performed in the galvanostatic mode between 0.01 V and 2.5 V *vs.* Na^+/Na . During the galvanostatic stage, the current density was 37.2 $\text{mA}\cdot\text{g}^{-1}$ for 5 cycles and then cycled at 372 $\text{mA}\cdot\text{g}^{-1}$. The densities were selected to correspond to C-rates of C/10 and C, respectively, taking into account a specific theoretical capacity C of 372 $\text{mAh}\cdot\text{g}^{-1}$. The specific capacities presented hereafter were calculated based on the hard carbon content of the electrodes (3-5 mg).

3. Results and discussion

3.1. Raw material characterization

The natural polyphenol extracts used for hard carbon synthesis are primarily composed of either condensed or hydrolysable tannins (see Table S1, SI). The FTIR spectra of the raw materials (Figure 1) provide information about the chemical bonds present in the precursors and reveal the chemical differences among them. For instance, all precursors exhibit similar FTIR spectra when varying the intensities of their bands. The intense absorption observed in the 3000–3700 cm^{-1} range is attributed to the –OH bonds on the aromatic rings of the tannins. Bands centred at approximately 2930 cm^{-1} are assigned to the vibration of the aliphatic –C–H– bonds associated with the polyphenol bridges. The band at approximately 1600 cm^{-1} corresponds to –C=C– stretching vibrations in the aromatic rings. In addition, phenolic C–C vibrations are observed in the 1400–1500 cm^{-1} range, whereas out-of-plane vibrations of aromatic –C–H are detected in the 600–900 cm^{-1} range. The presence of NO– bonds is also observed due to the initial precursor composition. Traces of nitrogen were detected by elemental analysis (Table S2, Supplementary Information). The major differences observed in the spectra depend on the nature of the precursor (*i.e.*, condensed or hydrolysable tannins). Hydrolysable tannins (chestnut and myrobalan extracts) exhibit intense bands at 1720 cm^{-1} and 1250 cm^{-1} . Both bands are associated with the C=O and =C–O stretching vibrations of tannic acid (gallotannin). The stretching vibration of –C–O–C– is also observed at 1100 cm^{-1} . On the other hand, polyphenols mainly composed of condensed tannins (catechu extract and both mimosa extracts) do not exhibit the previously mentioned bands. However, the catechu extract shows a band at approximately 1285 cm^{-1} , which is characteristic of flavonoid-based tannins and attributed to C–O stretching.^{54,55} This extract is the only one that exhibits a peak at 1140 cm^{-1} , which is associated with –C–O–C– stretching vibrations. In addition, all three condensed

tannins present a broad band centred at 1370 cm^{-1} , which is assigned to phenolic C–O stretching and O–H deformation.⁵⁵

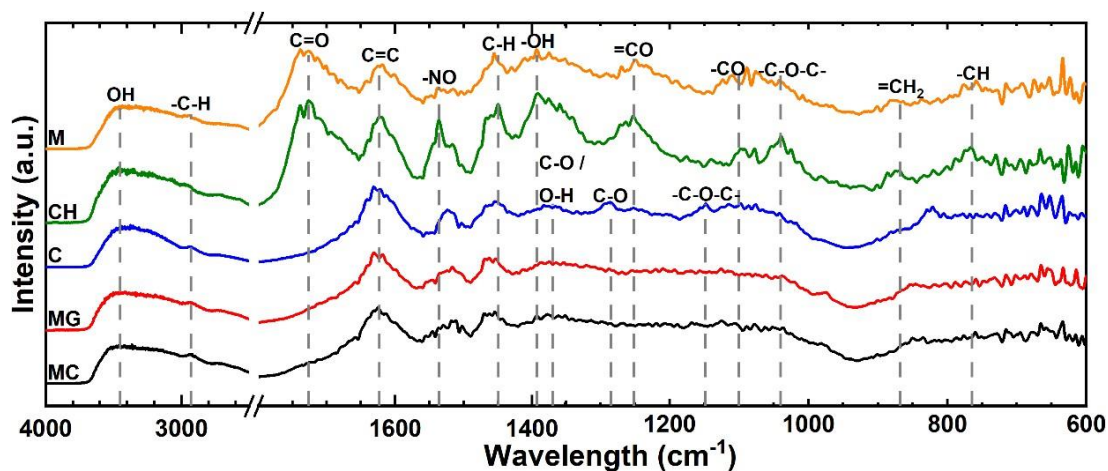


Figure 1. FTIR spectra of natural polyphenol extracts used as hard carbon precursors.

Thermal analysis techniques (TGA/DTG, presented in Figure 2) were used to evaluate the thermal conversion of the natural extracts into carbon, thus determining the carbon yield after the pyrolysis process. Raw materials containing condensed tannins (MC, MG and C) exhibit similar thermal behaviours, and both mimosa extracts become more stable as the temperature increases (Figure 2a). Three decomposition domains were identified on the DTG graph (Figure 2b) for all five natural extracts, despite the fact that those composed of hydrolysable tannins (CH and M) showed distinct thermal behaviours. The first decomposition step was observed in the 30-170 °C range and was associated with the release of adsorbed water or water formed by the condensation of –OH groups (between 8-10 wt.%). Then, a significant mass loss (between 27-40 wt.%) occurs in the 170-400 °C range, which could be attributed to the thermal decomposition of the main precursor constituents: either condensed or hydrolysable tannins for MC/MG/C and CH/M, respectively. Notably, myrobalan shows the lowest thermal stability, evidenced by the presence of a low temperature peak (~210 °C) and a second very intense peak at a higher temperature (310 °C). The higher oxygen and metallic impurity contents of this

precursor might increase the precursor decomposition rate (Table S2, Supporting Information). In addition, the liberation of H₂O, CO and CO₂ has previously been reported for similar hard carbon precursors²⁵ over the same temperature range. The last section of the DTG graph (after 400 °C) could be associated with the structural reorganization of the carbon and the thermal degradation of the remaining tannins. In particular, the CH precursor shows more decomposition in this domain than the other precursors.

The carbon yield also depends on the nature of the tannins. Extracts composed of condensed tannins exhibit higher carbon yields (above 40 wt.%) than extracts composed of hydrolysable tannins, such as myrobalan and chestnut extracts, which exhibit yields of 35 wt.% and 36 wt.%, respectively. This difference is due to the lower carbon content and higher oxygen and metallic contents of the latter (the elemental composition by EDX is presented in Table S2, Supporting Information). The carbon yield obtained with these vegetal extracts is greater than those obtained with other natural precursors such as cellulose, sucrose, and biomasses (~ 20 wt. %), allowing for faster synthesis of larger quantities and lower gas emissions during preparation. In fact, the yields are similar to synthetic polymers (PAN and phenol-based resins), with the added benefit of using sustainable and renewable resources.²⁸

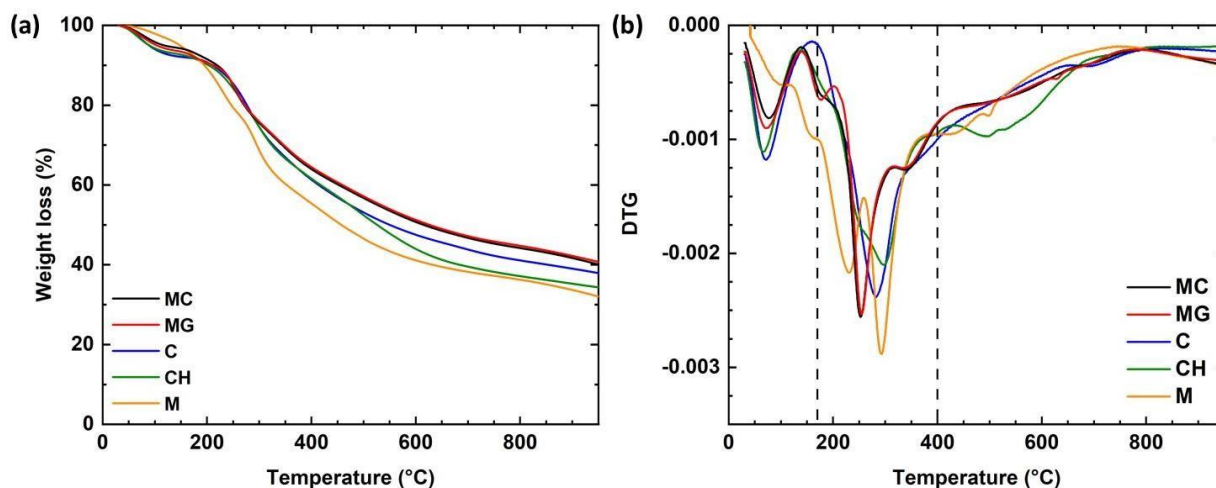


Figure 2. (a) TGA and (b) DTG curves of the different natural polyphenol extracts, recorded in an inert atmosphere.

3.2. Hard carbon structural characterization

Hard carbons were obtained by pyrolysis of natural extracts under an argon atmosphere. Because the carbon precursors were used as received, the morphology and particle size of the hard carbons were impacted only by the nature of the precursor (initial shape/size and composition). These properties play an important role in Na^+ insertion mechanisms. SEM images of the different hard carbons are presented in Figure 3. All materials exhibit a random morphology with a wide particle size distribution ranging from approximately 10-20 μm to hundreds of microns. Additionally, all hard carbons, with the exception of HC-C, contain some spherical particles that are hollow (broken spheres) in some cases. Indeed, the random particles appear to be shattered pieces of larger particles. The morphology of these materials is due to the nature of the precursor (Figure S1 of Supporting Information) and was not modified by the pyrolysis step. In addition, HC-C has the smallest particles ($\approx 2 \mu\text{m}$) compared to the other hard carbons which have particles of approximately 10-20 μm .

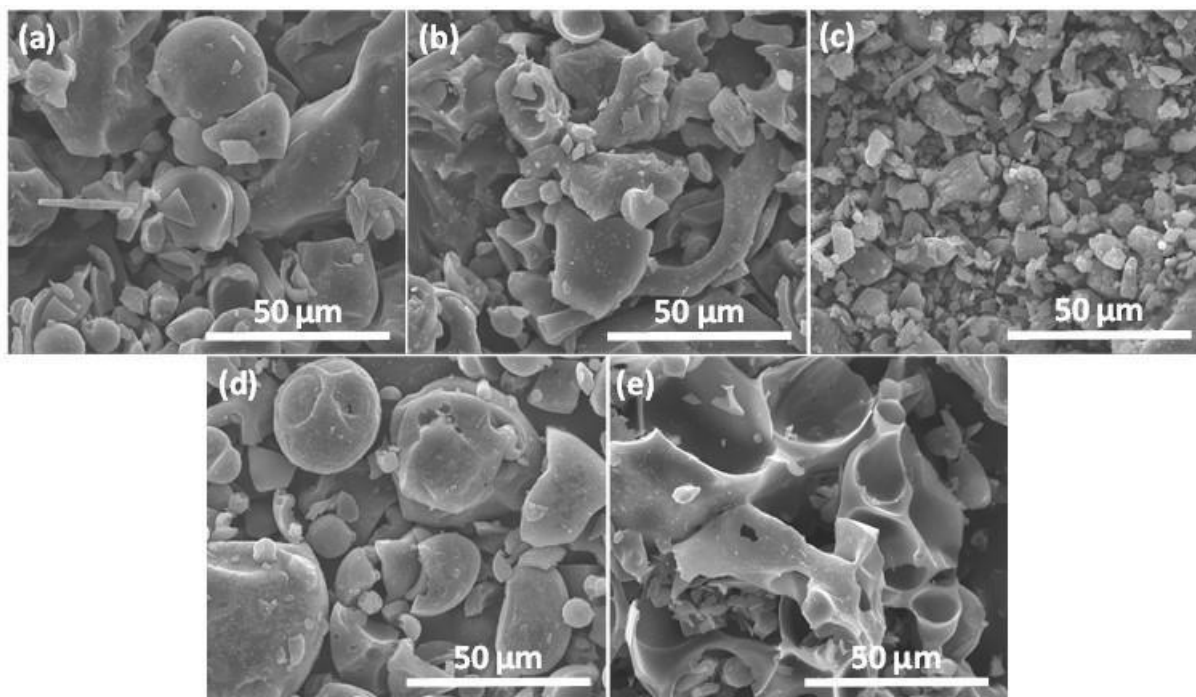


Figure 3. Scanning electron microscopy images of the synthesized hard carbons: (a) HC-MC; (b) HC-MG; (c) HC-C; (d) HC-CH; (e) HC-M.

The EDX technique, which offer deeper analysis penetration depth than other techniques such as XPS, was used to determine the composition of different hard carbons (Table 1). All materials are mainly composed of carbon (80-90 wt.%), followed by oxygen (7-14 wt.%). Interestingly, hard carbons obtained from hydrolysable tannins (HC-CH and HC-M), which exhibit lower pyrolysis yields than their condensed tannin counterparts (Figure 2 and Table 2), contain the most carbon (90 wt.%) and the least amount of the other elements. It is worth noting that the final compositions of the hydrolysable tannin-based hard carbons are quite similar, in contrast to their condensed tannin-based counterparts, which exhibit varied elemental ratios. The amount of oxygen varies between 10-14 wt.% and increases with the presence of metallic elements (*e.g.*, O wt.% and other elements wt.% are the highest for the HC-C sample). This might suggest that some elements form metal oxides and metal carbonates when they are bonded to oxygen. Further analysis (TGA and DTG curves recorded under dry air are presented

in Figure S2, Supporting Information) confirms that HC-C exhibits a slightly higher amount of residual ashes after pyrolysis (2.46 wt. %) while HC-MC and HC-CH show percentages below 2 wt.% (1.52 wt. % and 1.75 wt.% respectively, Table 1). The presence of elements such as Ca, K and S forming carbonates and oxides may impair the hard carbon electrochemical performance by promoting parasitic reactions during the cycling process, leading to lower iCEs, conductivities and cycle stabilities.^{31,38,56,57}

Table 1. EDX chemical analysis of different hard carbons and inorganic impurities amount determined by EDX and TGA under air.

Element (wt.%)	HC-MC	HC-MG	HC-C	HC-CH	HC-M
C	87.37	85.05	80.00	90.98	90.27
O	10.00	11.41	14.10	7.01	7.21
K	1.65	2.46	0.16	0.65	0.51
Ca	0.98	0.72	5.54	1.36	1.79
S	---	0.36	0.20	---	0.22
Inorganic impurities (EDX)	2.63	3.18	5.70	2.01	2.30
Inorganic impurities (TGA)	1.52	2.09	2.46	1.75	2.22

The material structure was further examined by X-ray diffraction, as shown in Figure 4a. All hard carbon patterns were characterized by 3 broad peaks centred at approximately 24°, 43.5° and 79° (2 θ), which correspond to the (002), (100) and (110) graphite diffraction planes, respectively. The broad shape of those peaks indicates the poor graphitization degree of these materials. The (002) plane provides information about the number of layers that compose the pseudographitic domains by determining the interlayer spacing (d_{002}) and the crystallite height (L_c), which are calculated by the Bragg and Scherrer equations, respectively. Moreover, the crystallite width (L_a) was determined, and all values are presented in Table 2. The hard carbons exhibit an interlayer spacing close to 3.6 Å, which is greater than that of graphite and enables

Na⁺ insertion. The HC-C sample has the smallest interlayer spacing of this series of hard carbons (3.55 Å), followed by HC-CH (3.57 Å). In addition, HC-C exhibits the largest crystallite width L_a (44 Å vs. 41 Å for the rest of the samples), indicating that its structure is the most organized of these materials. The crystallite height, L_c , of the materials ranges from 10 Å to 12 Å, and even though no trend was observed, all the hard carbons can stack up to 3 graphene layers on average in their pseudographitic domains.

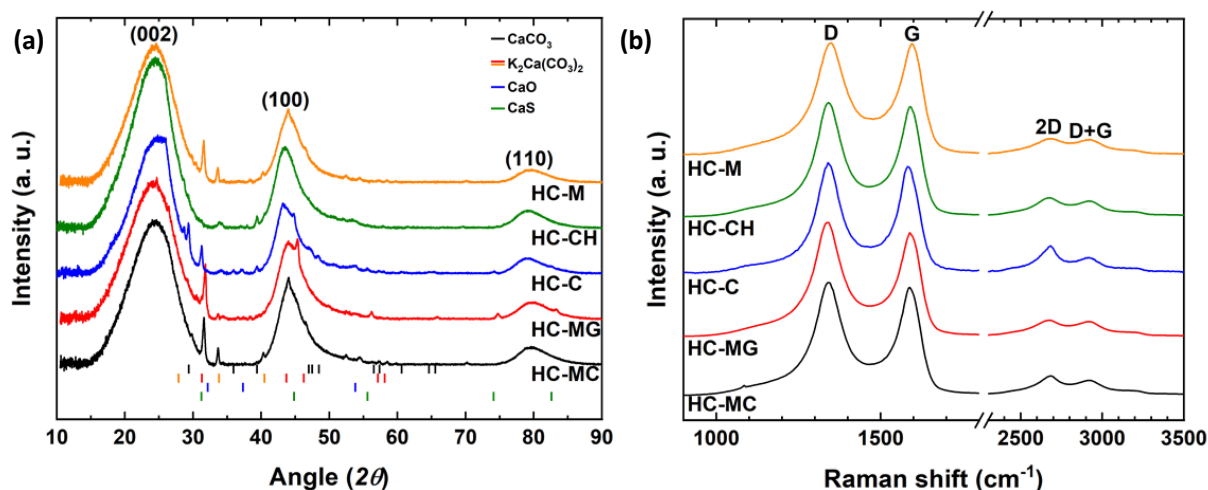


Figure 4. (a) Powder XRD patterns and (b) Raman spectra of the polyphenol-derived hard carbons.

Table 2. Summary of hard carbon physico-chemical properties.

Material	d_{002} ^a (Å)	L_c ^b (Å)	Nb layer s	L_a ^b (Å)	I_D/I_G ^c	N ₂ SSA ^d (m ² ·g ⁻¹)	CO ₂ SSA ^d (m ² ·g ⁻¹)	Density ^e (g·cm ⁻³)	C yield ^f (wt. %)	Inorganic compounds ^g (wt. %)
HC-MC	3.61	11	3.0	41	1.43	1.5	16.5	1.61	43.0	2.6
HC-MG	3.67	10	2.7	41	1.49	1.3	23.2	1.87	43.5	3.5
HC-C	3.55	12	3.6	44	1.26	6.9	16.2	1.51	40.0	5.9
HC-CH	3.57	12	3.4	41	1.36	2.2	15.0	1.36	36.0	2.0
HC-M	3.64	11	3.1	41	1.43	2.2	14.2	1.82	35.0	2.5

^a Derived from XRD data using the Bragg equation; ^b derived from XRD data using the Scherrer equation; ^c determined after Raman spectra fitting using Gaussian functions; ^d specific surface area determined by the BET model; ^e obtained from the He pycnometer; ^f calculated from ATG; ^g estimated from EDX analyses.

In addition to the hard carbon fingerprint, the XRD patterns reveal another five crystal phases that are associated with inorganic compounds. Although it was difficult to precisely identify and quantify the phases, the following phases were found: CaCO₃ (COD 9009668), CaO (COD 1011094), CaS (COD 9008606), K₂Ca(CO₃)₂-butschliite (COD 9009292) and K₂Ca(CO₃)₂-fairchildite (COD 9008300). This confirms the EDX hypothesis that carbonates and oxides form during heat treatment. It is worth noting that not all carbons exhibit the same crystal phases, as shown in Table S3 (Supporting Information). For instance, HC-C, which has the highest percentage of inorganic traces, can contain up to four compounds, while the other hard carbons contain only two compounds.

Any clear relation between the amount of impurities in these hard carbons and their influence on the d_{002} , L_c and L_a parameters is difficult to observe. However, the interlayer spacing (d_{002}) is precursor dependent, and the location of the impurities may or may not affect this parameter. Previous research has demonstrated that impurities located on the surface of carbon have little effect on the d_{002} value.^{38,56} In contrast, if those impurities are placed between the layers, d_{002} can be enlarged (in a similar way as for Li and Na insertion).³¹ Furthermore, research has proven that metals such as Ca, K, Fe and Si catalyse the transformation of amorphous carbon into graphite, and previous works have used CaCO₃ as a graphitization catalyst.⁵⁸⁻⁶⁰ The last compound was detected on three different hard carbons (Table S3, Supporting information). Among them, HC-C contains the highest amount of Ca and most likely also contains the highest amount of CaCO₃. The presence of these catalytic compounds often leads to local graphitization, thus forming graphitic domains and decreasing the interlayer spacing d_{002} . This phenomenon was confirmed by TEM micrographs, which will be shown later. However, it is

important to keep in mind that impurities may promote parasitic electrochemical reactions which will hinder the electrochemical performance of these hard carbons.

Moreover, Raman spectroscopy, which is a valuable technique for studying carbonaceous materials, highlights the degree of disorder in these materials. The hard carbon Raman spectra are plotted in Figure 4b, and all samples display two intense bands in the 1200-1700 cm^{-1} range. These peaks are associated with the disorder-induced band (D band centred at 1343 cm^{-1}) and the graphitic band (G band centred at 1590 cm^{-1}). In addition, two less intense bands were also observed in the 2300-3200 cm^{-1} range, corresponding to the 2D and D+G bands. The first indicates the degree of graphitization, while the latter indicates the presence of defects.

The disorder-induced band indicates the presence of impurities or defects in the graphitic crystal framework, and the I_D/I_G ratio, obtained by determining the surface under the D and G bands, is commonly used to evaluate the degree of disorder in graphitic and pseudo-graphitic materials. Here, the I_D/I_G ratios of the hard carbons were determined and are shown in Table 2. They allow for a comparison of these materials, and the results agree with the XRD analysis, which follows the same trend. For instance, the I_D/I_G ratios are greater than 1, which indicates that a larger contribution from the D band leads to highly disordered materials. However, when this series of hard carbons is compared, HC-C has the lowest I_D/I_G ratio (1.26), proving that it is less disordered than the others ($I_D/I_G \sim 1.4$). In contrast, HC-MG has the highest I_D/I_G ratio (1.49), as expected given its larger d_{002} and L_c parameters.

The HRTEM micrographs of the hard carbons, presented in Figure 5, reveal the disordered structure of these materials. HC-MG and HC-M are mainly composed of turbostratic domains, while the other hard carbons, notably HC-C (Figure 5e), exhibit clusters with more ordered graphite layers, thus confirming the catalytic effect of the residual inorganic compounds.

These better-ordered graphene layers form closed pores with graphitic walls, thus reducing the apparent density of the material. This type of porosity formation has been observed

previously.³⁸ The presence of these clusters is consistent with the Raman spectroscopy and XRD results, as samples with smaller d_{002} and I_D/I_G values are expected to have more pseudographitic domains than samples with larger d_{002} and I_D/I_G values.

In addition, local clusters of graphite layers composed of either straight or curved layers were observed, and the d-spacing between them was determined for the white square sections of Figure 5. The results follow the trend observed by XRD which indicates that HC-C has the shortest d-spacing and HC-MG has the largest d-spacing.

Three hard carbons were selected for complementary XPS surface chemistry analyses. Their elementary surface compositions, presented in Table 3, differ drastically from the EDX results (Table 1). The amount of carbon on the surface is lower than that in the bulk (*e.g.*, 90.98 wt.% in the bulk *vs.* 58.72 wt.% on the surface for HC-CH), implying that impurities are mainly located on the hard carbon surface. This phenomenon has already been observed in other natural-based hard carbons.^{38,56} It is worth mentioning that HC-C and HC-CH exhibit similar carbon and oxygen compositions (*i.e.*, ≈ 60 wt.% C and ≈ 20 wt.% O) on the surface, whereas HC-MG contains more carbon (71.9 wt.%) and less oxygen (10.5 wt.%). Thus, HC-C and HC-CH have more surface impurities than HC-MG.

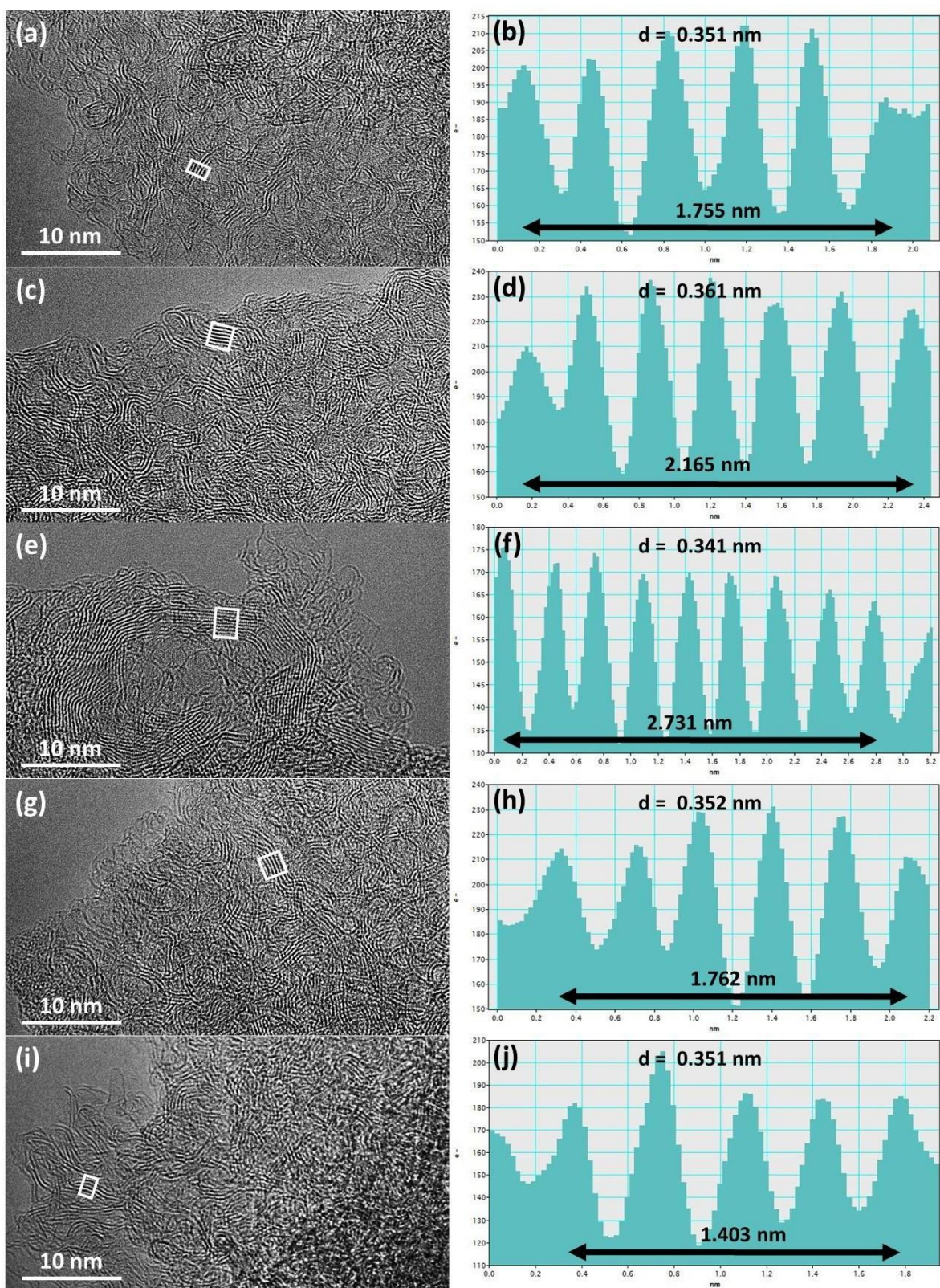


Figure 5. Transmission electron micrographs of synthesized hard carbons: (a) HC-MC; (c) HC-MG; (e) HC-C; (g) HC-CH; (i) HC-M. Hard carbon layer spacing of white squares (b) HC-MC; (d) HC-MG; (f) HC-C; (h) HC-CH; (j) HC-M.

Table 3. Surface chemical composition of hard carbons and C 1s repartition of components determined by XPS.

Hard carbon	Element (wt. %)						C 1s (at. %)					
	C	O	Ca	K	Cl	S	C sp ²	C-OR	C=O	COOR	Csp ³	CO ₃ ²⁻
HC-MG	71.86	10.49	3.11	10.50	2.66	1.38	64.34	5.84	1.63	1.51	3.69	2.27
HC-C	60.29	20.63	16.48	0.45	1.27	0.88	59.78	1.99	0.93	0.60	3.26	5.54
HC-CH	58.72	18.11	12.24	7.34	3.15	0.44	49.15	4.06	1.33	0.57	4.34	7.56

The C 1s high-resolution deconvoluted XPS spectra and the C 1s component repartition are presented in Figure 6 and Table 3, respectively (wide XPS spectra shown in Figure S3 of the Supporting Information). All three deconvoluted spectra show an intense and sharp peak at 284.4 eV, which is associated with sp² graphitic carbon and corresponds to the main carbon contribution, which can reach up to 64.3 at % for HC-MG. The other two hard carbons have a lower sp² carbon content (59.8 at. % and 49.1 at. % for HC-C and HC-CH, respectively). Moreover, smaller peaks in the 285-289 eV range demonstrate the presence of C sp³ and oxygenated functional groups such as ether (C-OR), carbonyl (C=O) and ester (COOR). The atomic concentration of sp³ defective carbon⁶¹ is similar (\approx 4 at. %) for all samples, which may lead to the trapping of Na⁺ ions on those defect sites during the first cycle.

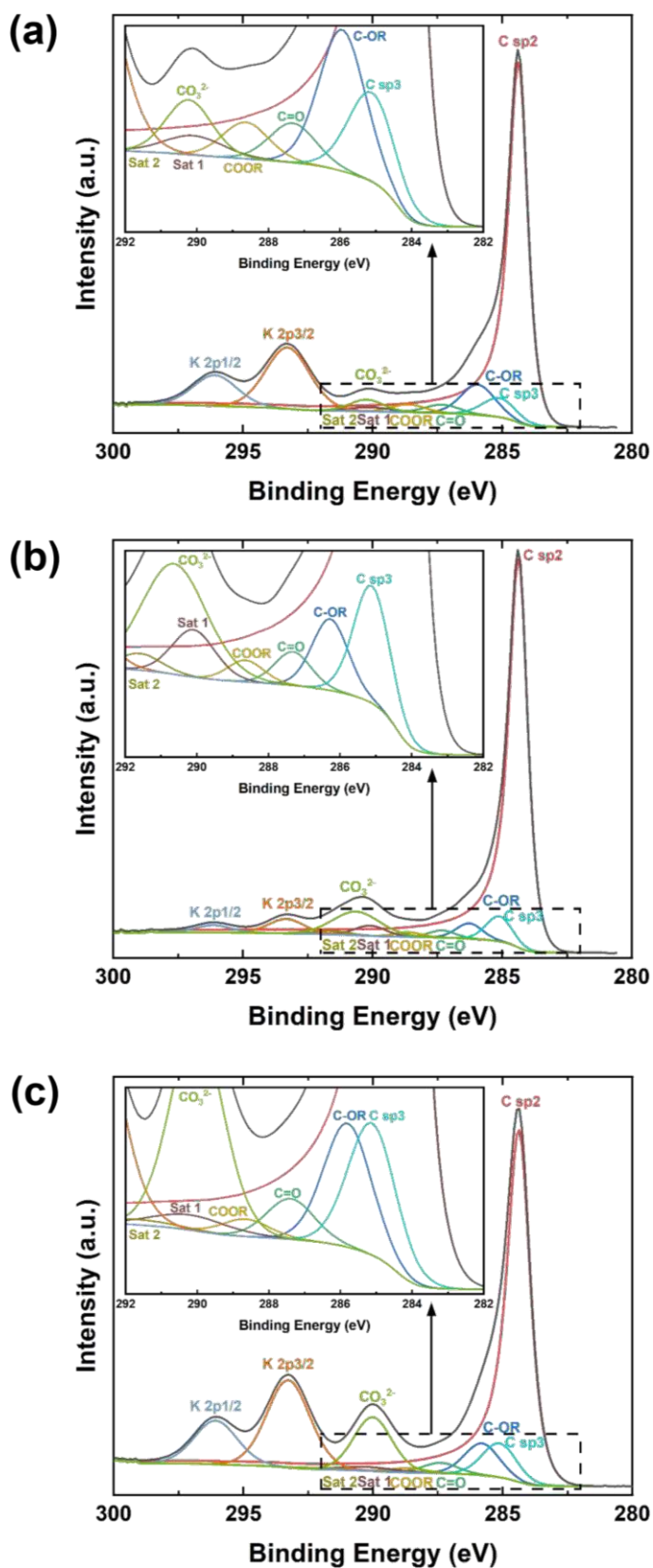


Figure 6. XPS C 1s high-resolution deconvoluted spectra of (a) HC-MG, (b) HC-C and (c) HC-CH.

On the other hand, oxygenated surface groups may participate in redox reactions with Na^+ ions, thus increasing the hard carbon capacity but inducing SEI formation.⁶² Because HC-MG has a higher concentration of these surface groups (9 at. %) and a higher amount of C sp^2 , it is expected to have a more significant capacity. In addition, two peaks associated with K 2p were observed, one centred at 293.3 eV and the other at 296.1 eV. These peaks have smaller intensities for HC-C, as this hard carbon contains less potassium than the others. The last XPS signal, centred at 290.3 eV, was attributed to the presence of carbonate (CO_3^{2-}), which agrees with the XRD results. Interestingly, the carbonate contribution is more important for HC-C and HC-CH (5.5 and 7.6 at. %, respectively). This implies that a greater concentration of catalytic compounds, such as CaCO_3 , are present, thus explaining the smaller d_{002} spacing and lower I_D/I_G ratios observed for these two materials (Table 2).

3.3. Hard carbon textural characterization

The porosity of the hard carbons was evaluated by N_2 and CO_2 physisorption assays, and the isotherms and pore size distributions are shown in Figure 7. The nitrogen adsorption-desorption isotherms exhibit a type II shape according to the IUPAC classification, which is characteristic of nonporous materials. The desorption branch does not reach the adsorption branch, indicating that some nitrogen is not desorbed and remains trapped in the narrow pores. The BET specific surface areas, which are determined by nitrogen physisorption (Table 2), were all below $7 \text{ m}^2 \cdot \text{g}^{-1}$. These values are beneficial for reducing irreversible reactions with the electrolyte and thus improving the iCE as open pores (determined by gas adsorption) irreversibly trap Na^+ ions. Hard carbons derived from the same natural precursor (hydrolysable or condensed tannins) have similar N_2 SSAs, with only the HC-C sample having a slightly higher SSA. One possible explanation is that this phenomenon is due to the residual compounds in HC-C, which lead to

activation phenomena and consequently to the creation of micro - and meso - porosity, as previously observed.^{38,56}

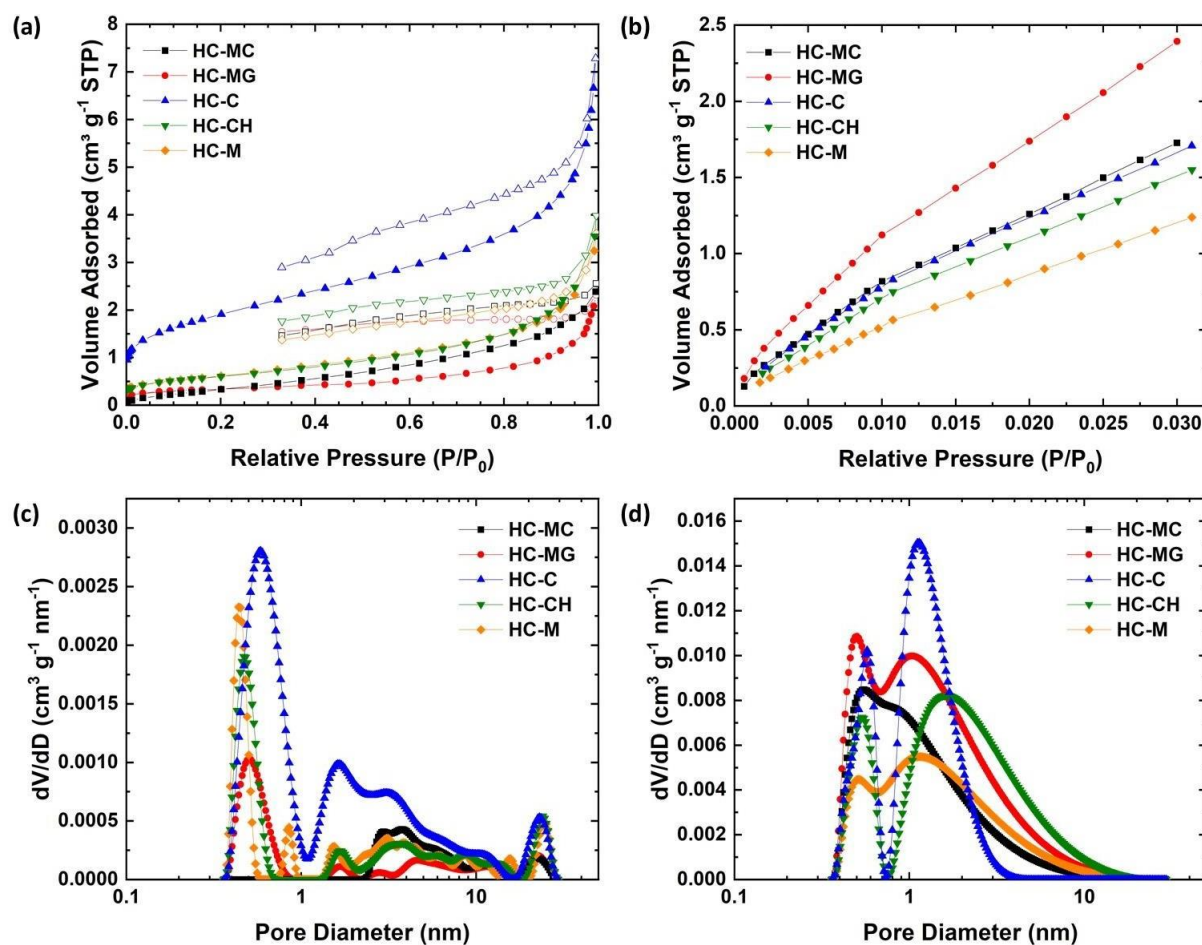


Figure 7. Hard carbon (a) N₂ and (b) CO₂ physisorption isotherms (filled and open symbols refer to the adsorption and desorption branches, respectively); hard carbon (c) N₂ and (d) CO₂ pore size distributions (Log scale) based on 2D-NLDFT theory (adsorption branch).

The 2D-NLDFT pore size distributions of all the hard carbons (Figure 7c) display multimodal mesoporous distributions in the 2-20 nm range, which confirms a larger mesoporous volume for HC-C, which could be associated with the pores having graphitic walls, as observed by TEM. Hard carbons exhibit different behaviours in the microporous domain; for instance, HC-MC does not appear to have any microporosity, while HC-M has a bimodal micropore

distribution centred at 0.45 and 0.85 nm. HC-MG, HC-CH and HC-C hard carbons all show monomodal micropore distributions with sizes centred between 0.5 and 0.6 nm.

CO₂ adsorption provides more information about the texture of the material because it can access narrower pores than nitrogen; thus, the specific surface areas determined by CO₂ are higher than those determined by N₂ (see Table 2). In fact, the CO₂ SSAs of these hard carbons range from 14 to 23 m²·g⁻¹, which are lower than those of other hard carbons obtained from biosourced precursors (CO₂ SSA > 100 m²·g⁻¹).^{25,31,56,63} This means that these hard carbons have a compact structure. Interestingly, HC-C, which has the highest N₂ SSA, does not exhibit the highest CO₂ SSA, which indicates that the ultramicroporosity contribution is less important in this sample than in the other samples, most likely due to the densification of the material via graphitization. Furthermore, CO₂ has been demonstrated to be an efficient gas to highlight the presence of ultramicroporosity (d < 0.7 nm) on hard carbon materials.⁶⁴ The 2D-NLDFT pore size distributions (Figure 7d) prove the presence of ultramicropores in all samples. In addition, all hard carbons exhibit bimodal pore size distributions centred between 0.5-0.6 nm and 1-2 nm.

The density of the hard carbons was determined using a gas pycnometer, with He selected as the displacement medium. Table 2 shows the measured densities, which range from 1.36 for HC-CH to 1.87 g·cm⁻³ for HC-MG. They have the following trend: $d_{\text{HC-CH}} < d_{\text{HC-C}} < d_{\text{HC-MC}} < d_{\text{HC-M}} < d_{\text{HC-MG}}$. These data were essential for determining the volume ratios of closed and open porosity (Table S4, Supporting Information). The closed porosity ratio follows the opposite trend as the density, which means that HC-CH with the lowest density (1.36 g·cm⁻³) shows the highest closed pore ratio (41 vol.%). Such values appear to be beneficial for Na⁺ storage because Na⁺ is stored between the graphene planes, defects and eventually the closed pores, according to previous work.^{2,24,53} Interestingly, HC-C and HC-CH, which possess a high graphitization degree (lowest d₀₀₂ and I_D/I_G values), have the lowest densities, leading to less compact

structures. Indeed, the graphitization process densifies the structure but in the same time the number of closed pores is increased; thus, closed pores are more prevalent herein because the graphitization is local. Moreover, all materials present a low open pore ratio ($R_{OP} < 1.7$ vol.%), which is beneficial for electrochemical performance, as a low open porosity percentage reduces the area in contact with the electrolyte. This limits the formation of SEIs and may also improve iCE values.

3.4. Hard carbon electrochemical performance

The hard carbon charge/discharge profiles are composed of two sections: a low voltage plateau region (0–0.1 V vs. Na⁺/Na) and a high voltage or slope region (V > 0.1 V vs. Na⁺/Na). Each section corresponds to a different Na⁺ ion storage mechanism, and previous studies have tried to determine whether the plateau is associated with Na⁺ adsorption on nanopores and defect sites or with the intercalation of Na⁺ between the graphene layers. While the traditional intercalation/slope-adsorption/plateau model¹⁸ is universally accepted, recent experimental and theoretical works^{2,53,65} have provided convincing evidence in favour of an alternative Na⁺ storage mechanism (*i.e.*, adsorption/slope-intercalation/plateau). The electrochemical results obtained here support the latter.

The hard carbon electrochemical behaviour *versus* Na⁺/Na was determined in half-cells by galvanostatic assays by applying a current density of $C = 372 \text{ mA} \cdot \text{g}^{-1}$. The first charge/discharge cycle of all five materials is presented in Figure 8a and shows the typical behaviour of the hard carbon sodiation/desodiation process.

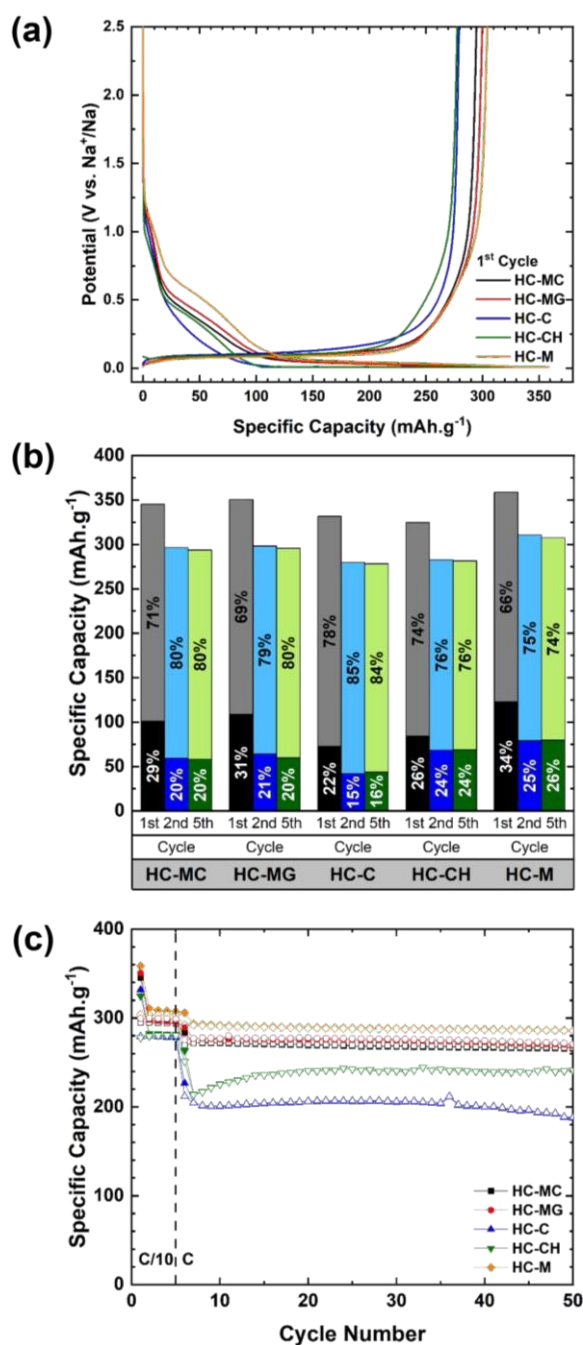


Figure 8. (a) Charge/discharge profiles of the hard carbons at a current rate of 37.2 mA·g⁻¹ (1st cycle); (b) Specific capacity of the 1st, 2nd and 5th discharges by sloping (V > 0.1 V vs. Na⁺/Na, bottom) and plateau (V < 0.1 V vs. Na⁺/Na, top) percentage contribution; (c) Cycling performance of the hard carbons at a current density of 372 mA·g⁻¹ (37.2 mA·g⁻¹ for the first 5 cycles); filled and open symbols refer to discharge and charge, respectively. All tests were performed over a voltage window of 0.01–2.5 V vs. Na⁺/Na.

The first discharge presents a shoulder at approximately 0.5-0.6 V vs. Na⁺/Na that does not appear on subsequent cycles (second cycle presented in Figure S4, Supporting Information). This electrochemical behaviour is associated with SEI layer formation, which stabilizes after the second cycle (cycle profiles at C/10 and C are presented in Figure S5, Supporting Information). The formation of this layer largely contributes to the irreversible capacity after the first cycle and dramatically affects the iCE. Other phenomena, such as irreversible sodium trapping in the carbon porosity and structure, may also contribute to the irreversibility of the first cycle.⁶⁶

These hard carbons have initial specific discharge capacities greater than 324 mAh·g⁻¹ and iCE values of approximately 85% (Table 4).

Table 4. Electrochemical performance of natural phenol-based hard carbons: 1st Ch/Dch cycle at a current density of 37.2 mA·g⁻¹ (C/10). The 6th and 50th Ch/Dch were cycled at a current density of 372 mA·g⁻¹ (C). It is important to note that the current density regime of the same coin cell was modified from C/10 to C at the 6th cycle.

Material	1 st C _{Dch} ^a (mAh·g ⁻¹)	1 st C _{Slope} ^b (mAh·g ⁻¹)	1 st C _{Plateau} ^c (mAh·g ⁻¹)	1 st C _{Ch} ^d (mAh·g ⁻¹)	iCE ^e (%)	6 th C _{Dc_h} ^a (mAh·g ⁻¹)	6 th C _{Dc_h} ^a /1 st C _{Dc_h} ^a (%)	50 th C _{Dc_h} ^a /6 th C _{Dc_h} ^a (%)
HC-MC	345.3	100.8	244.5	294.7	85.4	283.4	82.1	93.8
HC-MG	350.6	108.5	242.1	299.8	85.5	289.3	82.5	92.9
HC-C	331.7	72.5	259.2	279.2	84.2	226.6	68.3	81.7
HC-CH	324.6	84.3	240.3	277.7	85.6	263.2	81.1	91.7
HC-M	358.7	122.6	236.1	304.3	84.8	305.9	85.3	93.6

^a Discharge capacity; ^b slope capacity (C_{Dch} > 0.1 V vs. Na⁺/Na); ^c plateau capacity (C_{Dch} < 0.1 V vs. Na⁺/Na); ^d charge capacity; ^e initial Coulombic efficiency.

HC-MC, HC-MG and HC-M recover ~ 300 mAh·g⁻¹ upon charging, while HC-C and HC-CH recover ~278 mAh·g⁻¹. Although the HC-CH charge capacity is lower than that of the other

hard carbons, HC-CH exhibits one of the highest iCEs (*i.e.*, 85.6%). In general, the iCE values obtained for these materials are higher (84.2-85.6%) than those obtained by some hard carbons synthesized using phenolic resins and cycled even at lower current densities (*e.g.*, iCE of 60% for a hard carbon cycled at $20 \text{ mA}\cdot\text{g}^{-1}$)⁴⁶, and they are also comparable to other materials reported in the literature (Table 5). The slightly lower iCE for HC-C (84.2%) is due to the fact that this sample has the highest amount of residual inorganic compounds, a higher specific surface area, and the lowest d_{002} among these materials, promoting the formation of SEI and Na^+ trapping into narrower pseudographitic domains.

As previously mentioned, hard carbon galvanostatic profiles can be divided into two sections: the slope region and the plateau region, which correspond to capacities obtained in potential ranges of 0.1-2.5 V *vs.* Na^+/Na and 0-0.1 V *vs.* Na^+/Na , respectively. When the capacity contributions of the two sections are considered individually, the plateau region contributes the most (Table 4 and Figure 8b). All hard carbons have similar plateau capacities during the first discharge process, associated with 66-74% of the total discharge capacity, with values of approximately $240 \text{ mAh}\cdot\text{g}^{-1}$.

According to the “adsorption-intercalation” model, the intercalated Na^+ ions participate in the capacity observed at the low voltage plateau. For HC-C and HC-CH, the number of stacked graphenes layers is the highest one among all materials (Table 2) which would lead to higher capacity. However, the amount of carbon in each material is different and moreover, heterogeneous in the surface *vs.* bulk. In particular, the C% is the lowest one for HC-C material, therefore, less available sites are available for Na-ion storage. These parameters, *i.e.*, graphene interlayer space/staking and the amount of carbon impact Na-ion insertion, reason why, in the end, considering the structural and chemical composition differences in the materials, they all provide similar plateau capacity. The other contribution (22-34%) correspond to the slope capacity. In this region, Na-ion adsorption and SEI formation takes place and they might be

affected by several factors, such as the open porosity, surface chemistry (O content), defects and impurities. We have proposed previously that the slope capacity correlates with the adsorption of Na⁺ in carbon porosity and defects.^{23,53} As the specific surface area is rather similar for all materials, the amount of defects is more likely affecting the slope capacity. Indeed, the lowest I_D/I_G ratios are observed for HC-C and HC-CH (1.26 and 1.36), leading to lower slope capacity (72.5 and 84.3 mAh g⁻¹), whereas the other materials have higher I_D/I_G ratio (1.43 -1.49) and higher slope capacity (100.8 - 122.6 mAh g⁻¹). As this region is governed by surface processes, the amount of C in the surface become an important issue as well. This is lower for HC-C and HC-CH (~ 60 wt.%, XPS) compared to HC-MG (72 wt.%, XPS), which might also explain the slope capacities differences. Nevertheless, the oxygen functional groups and the impurities contributes probably in a major extent to the electrolyte decomposition and SEI formation. Therefore, the carbon properties impacting the slope capacity are multiple and more complex to precisely identify, considering both the Na-ion adsorption and the SEI formation occurring simultaneously. These two process varies with the cycling and we can observe that the slope contribution decreases while the plateau contribution increases in the 2nd cycle and remains stable in subsequent cycles. There is no clear evidence of a trend among these materials, as HC-CH has the highest slope retention (~ 81%), followed by HC-M (~ 64%). However, both materials used hydrolysable tannins as precursors and showed the highest carbon content (~ 90 wt%) and the least amount of oxygen (7 wt.%; EDX, Table 1). In terms of the plateau capacity of these materials, it is worth noting that hard carbons with larger interlayer spaces (d₀₀₂) and lower closed porosity ratios (R_{CP}) exhibit better capacity retention in this region (above 97% between the first two cycles). The other two hard carbons (HC-C and HC-CH), which both have lower d₀₀₂ values, retain approximately 90% of their initial plateau capacity.

Furthermore, the cycling performance of these hard carbons at C/10 and C is displayed in Figure 8c, and their Coulombic efficiencies are plotted in Figure S6 of the Supporting Information. The cycling behaviour at C/10 and C is material dependent. For instance, these hard carbons exhibit reversible capacities of approximately 300 mAh·g⁻¹, and all of them achieve Coulombic efficiencies close to 100% starting with the 2nd cycle. Besides, the materials are stable at C/10 (first five cycles) and remain stable at C in the case of HC-MC, HC-MG and HC-M. In contrast, a considerable decrease in the capacity was observed for HC-C and HC-CH when the regime was changed from C/10 to C (Figure 8c). These two carbons have the smallest d_{002} values (3.55 Å and 3.57 Å, respectively) and lower plateau capacity retentions. Such narrow spaces hinder the sodiation/desodiation process⁶⁷ at faster regimes, thus limiting Na⁺ insertion/extraction between the graphene layers. This issue continues during cycling for HC-C, which exhibits stability problems (faster capacity fading) when cycled at C. For instance, this hard carbon exhibits a capacity retention of 82% between the 6th and 50th cycles (cycling at C), while the other materials exhibit capacity retentions of approximately 92-93%.

One explanation could be the presence of residual inorganic compounds, which could lead to a less stable SEI.³⁸ Similarly, HC-CH presents a continuous capacity increase during the first 10-15 cycles at C (after the regime change). It could be attributed to slow SEI stabilization during transition from the C/10 rate to the C rate. However, this progressive increase could also be associated to slight structural changes upon cycling leading to a gradual change of the voltage profile. To better understand the precise reasons behind the observed behavior, supplementary analyses are necessary to be conducted.

Table 5. Physico-chemical and electrochemical properties of reported hard carbons derived from different phenolic resins; one material per article is presented (the best of the report).

Precursor	Morphology	HT (°C)	N ₂ SSA (m ² ·g ⁻¹)	d ₀₀₂ (Å)	C _{rate} (mA·g ⁻¹)	1 st C _{Dch} (mAh·g ⁻¹)	iCE (%)	Performance long cycling	Ref.
R/F resin	Porous xerogels	1000	593	n.a.	C/10	556	33	140 mAh·g ⁻¹ at C/10; 115 mAh·g ⁻¹ at C; 81 mAh·g ⁻¹ at 5 C after 200 cycles	6
R/F resin	Microspheres	1500	144	3.70	20	333	85	n.a.	39
R/F resin	Monoliths	1600	3.8	3.90	20	350	92	n.a.	40
P/F resin	Microspheres	1250	219.5	3.89	20	517	60.2	~160 mAh·g ⁻¹ at 100 mA·g ⁻¹ after 100 cycles	46
P/F resin	Microspheres	1100	35.3	3.89	20	394	84.7	197 mAh·g ⁻¹ at 100 mA·g ⁻¹ after 300 cycles	47
P/F resin	Closed pores	1550	1.44	3.91	30	446	86	~360 mAh·g ⁻¹ at 30 mA·g ⁻¹ after 40 cycles	68
A/F resin	Microspheres	1300	24	3.70	30	421.5	72	~280 mAh·g ⁻¹ at 50 mA·g ⁻¹ after 100 cycles	69

								181 mAh·g ⁻¹ at 100 mA·g ⁻¹	
								after 500 cycles	
								152 mAh·g ⁻¹ at 100 mA·g ⁻¹	
								after 160 cycles	
A/F resin-CNTs	Microspheres (like grapes)	900	35	3.42	100	606	33	95 mAh·g ⁻¹ at 1000 mA·g ⁻¹	70
								after 500 cycles	
R/G resin	Random	1300	34.8	3.99	20	367	88.6	160 mAh·g ⁻¹ at 1 A·g ⁻¹	41
								after 300 cycles	
Ph/G resin	Random	1300	7.9	3.98	C/10	350	76	230 mAh·g ⁻¹ at C/10	25
								after 40 cycles	
Ph/G resin	Microspheres	1500	3.5	3.80	C/50	295	92	n.a.	42
NP	Random	1500	2.2	3.64	C/10	359	84.8	286 mAh·g ⁻¹ at C	This work
								after 50 cycles	

R: Resorcinol; F: Formaldehyde; P: Phenol; A: Aminophenol; G: Glyoxylic acid; Ph: Phloroglucinol; CNT: Carbon nanotubes; NP: Natural Polyphenol; n.a.: Not available/not applicable; C=372 mA·g⁻¹.

Long cycling at C/10 was performed on HC-MC, HC-MG and HC-M (Figure S7 of Supporting Information), as these materials exhibited better electrochemical performances at C (higher capacities and better stability). As expected, these three hard carbons exhibited good stability at C/10, and their capacities and Coulombic efficiencies are similar. Thus, HC-MC,

HC-MG and HC-M exhibit good overall capacity retention and stability, as well as higher capacities than HC-C and HC-CH, which exhibit stability issues. These results make them promising materials for use as anodes in Na-ion batteries. It is important to note that the iCE values presented in this work are based on materials obtained through simple pyrolysis of natural precursors rather than complex synthesis methodologies.

4. Conclusions

In summary, five hard carbon materials were synthesized by simple pyrolysis at 1500 °C using natural polyphenols extracted from different plants. The precursors, which are mainly composed of either condensed or hydrolysable tannins, have carbon yields greater than 35 wt.%. The morphology of the hard carbons depends on the nature of the precursor and does not affect particularly affect the material performance. All hard carbons have a disordered structure and present some residual inorganic compounds, inherently induced by the parent precursor. The concentration of these inorganic compounds impacts the degree of graphitization of the materials. For instance, metal carbonates catalyse the graphitization process, thus decreasing the interlayer spacing and increasing the number of clusters with better-organized graphene layers. HC-C exhibits the most organized structure and has the lowest d_{002} and I_D/I_G values, as well as the highest amount of inorganic compounds. These characteristics, combined with the highest open porosity, hinder its electrochemical performance, promoting capacity fading. The interlayer spacing d_{002} is, in general, large enough to promote the intercalation of Na^+ ions. For example, myrobalan- and mimosa-based hard carbons, which have d_{002} values greater than 3.6 Å, exhibit good cycling stability, even after changing the current regime from C/10 to C ($C=372 \text{ mA}\cdot\text{g}^{-1}$). In general, the low surface area of the materials, as determined by N_2 and CO_2 physisorption, combined with the low open pore ratio, were favourable for limiting SEI formation, thus leading to high iCE values (above 84%). These materials also exhibit reversible

capacities of approximately $300 \text{ mAh}\cdot\text{g}^{-1}$ with good stability when cycled at $372 \text{ mA}\cdot\text{g}^{-1}$. This performance is similar to or even better than that of other hard carbons with tailored properties (*e.g.*, morphology, porosity) obtained through multiple and/or complex synthesis methods. In addition, the electrochemical behaviour of these materials is in accordance with the adsorption-intercalation mechanism for Na^+ storage. This simple approach provides new possibilities for the use of vegetal extracts with tannins as electrode materials for SIBs, as they provide a reliable, natural, renewable, nontoxic and low-cost resource for hard carbon production.

Associated content

Supporting Information

Price comparison (Table S1), elemental analysis (Table S2) and scanning electron microscopy images (Figure S1) of raw materials; crystal phases observed on hard carbons (Table S3); TGA under air of hard carbon materials (Figure S2); XPS wide spectra (Figure S3) and calculated volume ratios of closed porosity and open porosity (Table S4) of hard carbons; discharge capacity contributions for the slope region and the plateau region at different cycles (Table S5); charge/discharge profiles of the hard carbons during the 2nd, 5th, 10th and 50th cycles (Figure S4 and Figure S5); Coulombic efficiency of the hard carbons (Figure S6) and cycling performance of hard carbons at a current density of $37.2 \text{ mA}\cdot\text{g}^{-1}$ (Figure S7).

Author information

Notes

There are no conflicts of interest to declare.

Acknowledgements

This work was financially supported by the European Union's Horizon 2020 Program (project NAIMA, call: LC-BAT-02, Contract no. 875629). It was realized in the frame of the

RS2E network (French research network on electrochemical energy storage) and the laboratory of excellency for electrochemical energy storage (STORE-EX). The authors thank Dr. Loïc Vidal (HRTEM images), Dr. Jean-Marc Le Meins (XRD analysis) and Dr. Philippe Fioux (XPS analysis) for technical support via IS2M technical platforms. The authors also acknowledge Omar Rahmouni for help with the experimental work.

References

- (1) Bresser, D.; Buchholz, D.; Moretti, A.; Varzi, A.; Passerini, S. Alternative Binders for Sustainable Electrochemical Energy Storage – the Transition to Aqueous Electrode Processing and Bio-Derived Polymers. *Energy Environ. Sci.* **2018**, *11* (11), 3096–3127. <https://doi.org/10.1039/C8EE00640G>.
- (2) Bommier, C.; Mitlin, D.; Ji, X. Internal Structure – Na Storage Mechanisms – Electrochemical Performance Relations in Carbons. *Prog. Mater. Sci.* **2018**, *97*, 170–203. <https://doi.org/https://doi.org/10.1016/j.pmatsci.2018.04.006>.
- (3) Ozawa, K.; Editor. *Lithium Ion Rechargeable Batteries.*; Wiley-VCH Verlag GmbH & Co. KGaA, 2009. <https://doi.org/10.1002/9783527629022>.
- (4) Hirsh, H. S.; Li, Y.; Tan, D. H. S.; Zhang, M.; Zhao, E.; Meng, Y. S. Sodium-Ion Batteries Paving the Way for Grid Energy Storage. *Adv. Energy Mater.* **2020**, *10* (32), 2001274. <https://doi.org/https://doi.org/10.1002/aenm.202001274>.
- (5) Dahbi, M.; Yabuuchi, N.; Kubota, K.; Tokiwa, K.; Komaba, S. Negative Electrodes for Na-Ion Batteries. *Phys. Chem. Chem. Phys.* **2014**, *16* (29), 15007–15028. <https://doi.org/10.1039/C4CP00826J>.
- (6) Cuesta, N.; Cameán, I.; Arenillas, A.; García, A. B. Exploring the Application of Carbon

- Xerogels as Anodes for Sodium-Ion Batteries. *Microporous Mesoporous Mater.* **2020**, *308*, 110542. <https://doi.org/https://doi.org/10.1016/j.micromeso.2020.110542>.
- (7) Han, M. H.; Gonzalo, E.; Singh, G.; Rojo, T. A Comprehensive Review of Sodium Layered Oxides: Powerful Cathodes for Na-Ion Batteries. *Energy Environ. Sci.* **2015**, *8* (1), 81–102. <https://doi.org/10.1039/C4EE03192J>.
- (8) Clément, R. J.; Bruce, P. G.; Grey, C. P. Review—Manganese-Based P2-Type Transition Metal Oxides as Sodium-Ion Battery Cathode Materials. *J. Electrochem. Soc.* **2015**, *162* (14), A2589–A2604. <https://doi.org/10.1149/2.0201514jes>.
- (9) Zhang, Z.; Du, Y.; Wang, Q.-C.; Xu, J.; Zhou, Y.-N.; Bao, J.; Shen, J.; Zhou, X. A Yolk–Shell-Structured FePO₄ Cathode for High-Rate and Long-Cycling Sodium-Ion Batteries. *Angew. Chemie Int. Ed.* **2020**, *59* (40), 17504–17510. <https://doi.org/https://doi.org/10.1002/anie.202008318>.
- (10) Xiang, X.; Zhang, K.; Chen, J. Recent Advances and Prospects of Cathode Materials for Sodium-Ion Batteries. *Adv. Mater.* **2015**, *27* (36), 5343–5364. <https://doi.org/https://doi.org/10.1002/adma.201501527>.
- (11) Yabuuchi, N.; Komaba, S. Recent Research Progress on Iron- and Manganese-Based Positive Electrode Materials for Rechargeable Sodium Batteries. *Sci. Technol. Adv. Mater.* **2014**, *15* (4), 43501. <https://doi.org/10.1088/1468-6996/15/4/043501>.
- (12) Wang, L.; Song, J.; Qiao, R.; Wray, L. A.; Hossain, M. A.; Chuang, Y.-D.; Yang, W.; Lu, Y.; Evans, D.; Lee, J.-J.; Vail, S.; Zhao, X.; Nishijima, M.; Kakimoto, S.; Goodenough, J. B. Rhombohedral Prussian White as Cathode for Rechargeable Sodium-Ion Batteries. *J. Am. Chem. Soc.* **2015**, *137* (7), 2548–2554. <https://doi.org/10.1021/ja510347s>.

- (13) Wang, Z.; Selbach, S. M.; Grande, T. Van Der Waals Density Functional Study of the Energetics of Alkali Metal Intercalation in Graphite. *RSC Adv.* **2014**, *4* (8), 4069–4079. <https://doi.org/10.1039/C3RA47187J>.
- (14) Okamoto, Y. Density Functional Theory Calculations of Alkali Metal (Li, Na, and K) Graphite Intercalation Compounds. *J. Phys. Chem. C* **2014**, *118* (1), 16–19. <https://doi.org/10.1021/jp4063753>.
- (15) Moriwake, H.; Kuwabara, A.; Fisher, C. A. J.; Ikuhara, Y. Why Is Sodium-Intercalated Graphite Unstable? *RSC Adv.* **2017**, *7* (58), 36550–36554. <https://doi.org/10.1039/C7RA06777A>.
- (16) Guan, Z.; Shen, X.; Yu, R.; Wang, Z.; Chen, L. Chemical Intercalation of Solvated Sodium Ions in Graphite. *Electrochim. Acta* **2016**, *222*, 1365–1370. <https://doi.org/https://doi.org/10.1016/j.electacta.2016.11.112>.
- (17) Jache, B.; Adelhelm, P. Use of Graphite as a Highly Reversible Electrode with Superior Cycle Life for Sodium-Ion Batteries by Making Use of Co-Intercalation Phenomena. *Angew. Chemie Int. Ed.* **2014**, *53* (38), 10169–10173. <https://doi.org/https://doi.org/10.1002/anie.201403734>.
- (18) Stevens, D. A.; Dahn, J. R. The Mechanisms of Lithium and Sodium Insertion in Carbon Materials. *J. Electrochem. Soc.* **2001**, *148* (8), A803. <https://doi.org/10.1149/1.1379565>.
- (19) Wang, Q.; Ge, X.; Xu, J.; Du, Y.; Zhao, X.; Si, L.; Zhou, X. Fabrication of Microporous Sulfur-Doped Carbon Microtubes for High-Performance Sodium-Ion Batteries. *ACS Appl. Energy Mater.* **2018**, *1* (11), 6638–6645. <https://doi.org/10.1021/acsaem.8b01690>.
- (20) Xu, X.; Si, L.; Zhou, X.; Tu, F.; Zhu, X.; Bao, J. Chemical Bonding between Antimony

- and Ionic Liquid-Derived Nitrogen-Doped Carbon for Sodium-Ion Battery Anode. *J. Power Sources* **2017**, *349*, 37–44.
<https://doi.org/https://doi.org/10.1016/j.jpowsour.2017.03.026>.
- (21) Bin Cao, X. L. Recent Progress on Carbon-Based Anode Materials for Na-Ion Batteries. *Acta Physico-Chimica Sinica*. pp 1905000–1905003.
- (22) Dahn, J. R.; Xing, W.; Gao, Y. The “Falling Cards Model” for the Structure of Microporous Carbons. *Carbon N. Y.* **1997**, *35* (6), 825–830.
[https://doi.org/https://doi.org/10.1016/S0008-6223\(97\)00037-7](https://doi.org/https://doi.org/10.1016/S0008-6223(97)00037-7).
- (23) Zhang, B.; Ghimbeu, C. M.; Laberty, C.; Vix-Guterl, C.; Tarascon, J.-M. Correlation Between Microstructure and Na Storage Behavior in Hard Carbon. *Adv. Energy Mater.* **2016**, *6* (1), 1501588. <https://doi.org/https://doi.org/10.1002/aenm.201501588>.
- (24) Anji Reddy, M.; Helen, M.; Groß, A.; Fichtner, M.; Euchner, H. Insight into Sodium Insertion and the Storage Mechanism in Hard Carbon. *ACS Energy Lett.* **2018**, *3* (12), 2851–2857. <https://doi.org/10.1021/acsenergylett.8b01761>.
- (25) Beda, A.; Taberna, P.-L.; Simon, P.; Matei Ghimbeu, C. Hard Carbons Derived from Green Phenolic Resins for Na-Ion Batteries. *Carbon N. Y.* **2018**, *139*, 248–257.
<https://doi.org/https://doi.org/10.1016/j.carbon.2018.06.036>.
- (26) Bommier, C.; Surta, T. W.; Dolgos, M.; Ji, X. New Mechanistic Insights on Na-Ion Storage in Nongraphitizable Carbon. *Nano Lett.* **2015**, *15* (9), 5888–5892.
<https://doi.org/10.1021/acs.nanolett.5b01969>.
- (27) Fondard, J.; Irisarri, E.; Courrèges, C.; Palacin, M. R.; Ponrouch, A.; Dedryvère, R. SEI Composition on Hard Carbon in Na-Ion Batteries After Long Cycling: Influence of Salts

- (NaPF₆, NaTFSI) and Additives (FEC, DMCF). *J. Electrochem. Soc.* **2020**, *167* (7), 70526. <https://doi.org/10.1149/1945-7111/ab75fd>.
- (28) del Mar Saavedra Rios, C.; Beda, A.; Simonin, L.; Matei Ghimbeu, C. Hard Carbon for Na-Ion Batteries: From Synthesis to Performance and Storage Mechanism. *Na-ion Batteries*. April 20, 2021, pp 101–146. <https://doi.org/https://doi.org/10.1002/9781119818069.ch3>.
- (29) Chen, D.; Luo, K.; Yang, Z.; Zhong, Y.; Wu, Z.; Song, Y.; Chen, G.; Wang, G.; Zhong, B.; Guo, X. Direct Conversion of Ester Bond-Rich Waste Plastics into Hard Carbon for High-Performance Sodium Storage. *Carbon N. Y.* **2021**, *173*, 253–261. <https://doi.org/https://doi.org/10.1016/j.carbon.2020.11.004>.
- (30) Bai, Y.; Wang, Z.; Wu, C.; Xu, R.; Wu, F.; Liu, Y.; Li, H.; Li, Y.; Lu, J.; Amine, K. Hard Carbon Originated from Polyvinyl Chloride Nanofibers As High-Performance Anode Material for Na-Ion Battery. *ACS Appl. Mater. Interfaces* **2015**, *7* (9), 5598–5604. <https://doi.org/10.1021/acsami.5b00861>.
- (31) Beda, A.; Le Meins, J.-M.; Taberna, P.-L.; Simon, P.; Matei Ghimbeu, C. Impact of Biomass Inorganic Impurities on Hard Carbon Properties and Performance in Na-Ion Batteries. *Sustain. Mater. Technol.* **2020**, *26*, e00227. <https://doi.org/https://doi.org/10.1016/j.susmat.2020.e00227>.
- (32) Nita, C.; Zhang, B.; Dentzer, J.; Matei Ghimbeu, C. Hard Carbon Derived from Coconut Shells, Walnut Shells, and Corn Silk Biomass Waste Exhibiting High Capacity for Na-Ion Batteries. *J. Energy Chem.* **2021**, *58*, 207–218. <https://doi.org/https://doi.org/10.1016/j.jechem.2020.08.065>.
- (33) Zhang, F.; Yao, Y.; Wan, J.; Henderson, D.; Zhang, X.; Hu, L. High Temperature

- Carbonized Grass as a High Performance Sodium Ion Battery Anode. *ACS Appl. Mater. Interfaces* **2017**, *9* (1), 391–397. <https://doi.org/10.1021/acsami.6b12542>.
- (34) Wang, P.; Zhu, X.; Wang, Q.; Xu, X.; Zhou, X.; Bao, J. Kelp-Derived Hard Carbons as Advanced Anode Materials for Sodium-Ion Batteries. *J. Mater. Chem. A* **2017**, *5* (12), 5761–5769. <https://doi.org/10.1039/C7TA00639J>.
- (35) Yamamoto, H.; Muratsubaki, S.; Kubota, K.; Fukunishi, M.; Watanabe, H.; Kim, J.; Komaba, S. Synthesizing Higher-Capacity Hard-Carbons from Cellulose for Na- and K-Ion Batteries. *J. Mater. Chem. A* **2018**, *6* (35), 16844–16848. <https://doi.org/10.1039/C8TA05203D>.
- (36) Irisarri, E.; Amini, N.; Tennison, S.; Ghimbeu, C. M.; Gorka, J.; Vix-Guterl, C.; Ponrouch, A.; Palacin, M. R. Optimization of Large Scale Produced Hard Carbon Performance in Na-Ion Batteries: Effect of Precursor, Temperature and Processing Conditions. *J. Electrochem. Soc.* **2018**, *165* (16), A4058–A4066. <https://doi.org/10.1149/2.1171816jes>.
- (37) Yang, J.; Zhou, X.; Li, J.; Zou, Y.; Tang, J. Study of Nano-Porous Hard Carbons as Anode Materials for Lithium Ion Batteries. *Mater. Chem. Phys.* **2012**, *135* (2), 445–450. <https://doi.org/https://doi.org/10.1016/j.matchemphys.2012.05.006>.
- (38) Conder, J.; Vaultot, C.; Marino, C.; Villevieille, C.; Ghimbeu, C. M. Chitin and Chitosan—Structurally Related Precursors of Dissimilar Hard Carbons for Na-Ion Battery. *ACS Appl. Energy Mater.* **2019**, *2* (7), 4841–4852. <https://doi.org/10.1021/acsaem.9b00545>.
- (39) Asfaw, H. D.; Tai, C.-W.; Valvo, M.; Younesi, R. Facile Synthesis of Hard Carbon Microspheres from Polyphenols for Sodium-Ion Batteries: Insight into Local Structure

- and Interfacial Kinetics. *Mater. Today Energy* **2020**, *18*, 100505. <https://doi.org/https://doi.org/10.1016/j.mtener.2020.100505>.
- (40) Hasegawa, G.; Kanamori, K.; Kannari, N.; Ozaki, J.; Nakanishi, K.; Abe, T. Hard Carbon Anodes for Na-Ion Batteries: Toward a Practical Use. *ChemElectroChem* **2015**, *2* (12), 1917–1920. <https://doi.org/https://doi.org/10.1002/celec.201500412>.
- (41) Wang, J.; Lv, W.; Ren, Q.; Yan, L.; Zhang, L.; Shi, Z. High-Performance Hard Carbon Anode Prepared via an Ingenious Green-Hydrothermal Route. *Appl. Surf. Sci.* **2021**, *558*, 149824. <https://doi.org/https://doi.org/10.1016/j.apsusc.2021.149824>.
- (42) Beda, A.; Rabuel, F.; Morcrette, M.; Knopf, S.; Taberna, P.-L.; Simon, P.; Matei Ghimbeu, C. Hard Carbon Key Properties Allow for the Achievement of High Coulombic Efficiency and High Volumetric Capacity in Na-Ion Batteries. *J. Mater. Chem. A* **2021**, *9* (3), 1743–1758. <https://doi.org/10.1039/D0TA07687B>.
- (43) Kamiyama, A.; Kubota, K.; Nakano, T.; Fujimura, S.; Shiraishi, S.; Tsukada, H.; Komaba, S. High-Capacity Hard Carbon Synthesized from Macroporous Phenolic Resin for Sodium-Ion and Potassium-Ion Battery. *ACS Appl. Energy Mater.* **2020**, *3* (1), 135–140. <https://doi.org/10.1021/acsaem.9b01972>.
- (44) Lin, X.; Liu, Y.; Tan, H.; Zhang, B. Advanced Lignin-Derived Hard Carbon for Na-Ion Batteries and a Comparison with Li and K Ion Storage. *Carbon N. Y.* **2020**, *157*, 316–323. <https://doi.org/https://doi.org/10.1016/j.carbon.2019.10.045>.
- (45) Rey-Raap, N.; Szczurek, A.; Fierro, V.; Celzard, A.; Menéndez, J. A.; Arenillas, A. Advances in Tailoring the Porosity of Tannin-Based Carbon Xerogels. *Ind. Crops Prod.* **2016**, *82*, 100–106. <https://doi.org/https://doi.org/10.1016/j.indcrop.2015.12.001>.

- (46) Wang, H.; Shi, Z.; Jin, J.; Chong, C.; Wang, C. Properties and Sodium Insertion Behavior of Phenolic Resin-Based Hard Carbon Microspheres Obtained by a Hydrothermal Method. *J. Electroanal. Chem.* **2015**, *755*, 87–91. <https://doi.org/10.1016/j.jelechem.2015.07.032>.
- (47) Zhang, G.; Zhang, L.; Ren, Q.; Yan, L.; Zhang, F.; Lv, W.; Shi, Z. Tailoring a Phenolic Resin Precursor by Facile Pre-Oxidation Tactics to Realize a High-Initial-Coulombic-Efficiency Hard Carbon Anode for Sodium-Ion Batteries. *ACS Appl. Mater. Interfaces* **2021**, *13* (27), 31650–31659. <https://doi.org/10.1021/acsami.1c06168>.
- (48) Das, A. K.; Islam, M. N.; Faruk, M. O.; Ashaduzzaman, M.; Dungani, R. Review on Tannins: Extraction Processes, Applications and Possibilities. *South African J. Bot.* **2020**, *135*, 58–70. <https://doi.org/10.1016/j.sajb.2020.08.008>.
- (49) Sanchez-Sanchez, A.; Izquierdo, M. T.; Mathieu, S.; González-Álvarez, J.; Celzard, A.; Fierro, V. Outstanding Electrochemical Performance of Highly N- and O-Doped Carbons Derived from Pine Tannin. *Green Chem.* **2017**, *19* (11), 2653–2665. <https://doi.org/10.1039/C7GC00491E>.
- (50) Celzard, A.; Fierro, V. “Green”, Innovative, Versatile and Efficient Carbon Materials from Polyphenolic Plant Extracts. *Carbon N. Y.* **2020**, *167*, 792–815. <https://doi.org/10.1016/j.carbon.2020.05.053>.
- (51) Amaral-Labat, G.; Szczurek, A.; Fierro, V.; Stein, N.; Boulanger, C.; Pizzi, A.; Celzard, A. Pore Structure and Electrochemical Performances of Tannin-Based Carbon Cryogels. *Biomass and Bioenergy* **2012**, *39*, 274–282. <https://doi.org/10.1016/j.biombioe.2012.01.019>.
- (52) Matei Ghimbeu, C.; Beda, A.; Taberna, P.-L.; Simon, P.; Morcrette, M.; Rabuel, F.

Matériau Carboné, Son Utilisation Dans Des Batteries, Son Procédé de Fabrication et Une Électrode Le Comprenant. FR3104565, June 18, 2021.

- (53) Matei Ghimbeu, C.; Górká, J.; Simone, V.; Simonin, L.; Martinet, S.; Vix-Guterl, C. Insights on the Na⁺ Ion Storage Mechanism in Hard Carbon: Discrimination between the Porosity, Surface Functional Groups and Defects. *Nano Energy* **2018**, *44*, 327–335. <https://doi.org/https://doi.org/10.1016/j.nanoen.2017.12.013>.
- (54) Edelmann, A.; Lendl, B. Toward the Optical Tongue: Flow-Through Sensing of Tannin–Protein Interactions Based on FTIR Spectroscopy. *J. Am. Chem. Soc.* **2002**, *124* (49), 14741–14747. <https://doi.org/10.1021/ja026309v>.
- (55) Falcão, L.; Araújo, M. E. M. Application of ATR–FTIR Spectroscopy to the Analysis of Tannins in Historic Leathers: The Case Study of the Upholstery from the 19th Century Portuguese Royal Train. *Vib. Spectrosc.* **2014**, *74*, 98–103. <https://doi.org/https://doi.org/10.1016/j.vibspec.2014.08.001>.
- (56) Matei Ghimbeu, C.; Zhang, B.; Martinez de Yuso, A.; Réty, B.; Tarascon, J.-M. Valorizing Low Cost and Renewable Lignin as Hard Carbon for Na-Ion Batteries: Impact of Lignin Grade. *Carbon N. Y.* **2019**, *153*, 634–647. <https://doi.org/https://doi.org/10.1016/j.carbon.2019.07.026>.
- (57) Saavedra Rios, C. D.; Simonin, L.; Geyer, A. D.; Matei Ghimbeu, C.; Dupont, C. Unraveling the Properties of Biomass-Derived Hard Carbons upon Thermal Treatment for a Practical Application in Na-Ion Batteries. *Energies*. 2020, p 3513. <https://doi.org/10.3390/en13143513>.
- (58) Hirano, S.; Inagaki, M.; Saito, H. Cooperative Accelerating Effect of Calcium Carbonate and Gaseous Nitrogen on Graphitization of Carbon. *Carbon N. Y.* **1979**, *17* (5), 395–398.

[https://doi.org/https://doi.org/10.1016/0008-6223\(79\)90053-8](https://doi.org/https://doi.org/10.1016/0008-6223(79)90053-8).

- (59) Xie, Q.; Qu, S.; Zhang, Y.; Zhao, P. Nitrogen-Enriched Graphene-like Carbon Architecture with Tunable Porosity Derived from Coffee Ground as High Performance Anodes for Lithium Ion Batteries. *Appl. Surf. Sci.* **2021**, *537*, 148092. <https://doi.org/https://doi.org/10.1016/j.apsusc.2020.148092>.
- (60) Yang, G.; Han, H.; Li, T.; Du, C. Synthesis of Nitrogen-Doped Porous Graphitic Carbons Using Nano-CaCO₃ as Template, Graphitization Catalyst, and Activating Agent. *Carbon N. Y.* **2012**, *50* (10), 3753–3765. <https://doi.org/https://doi.org/10.1016/j.carbon.2012.03.050>.
- (61) Xiao, L.; Lu, H.; Fang, Y.; Sushko, M. L.; Cao, Y.; Ai, X.; Yang, H.; Liu, J. Low-Defect and Low-Porosity Hard Carbon with High Coulombic Efficiency and High Capacity for Practical Sodium Ion Battery Anode. *Adv. Energy Mater.* **2018**, *8* (20), 1703238. <https://doi.org/https://doi.org/10.1002/aenm.201703238>.
- (62) Yan, D.; Yu, C.; Zhang, X.; Qin, W.; Lu, T.; Hu, B.; Li, H.; Pan, L. Nitrogen-Doped Carbon Microspheres Derived from Oatmeal as High Capacity and Superior Long Life Anode Material for Sodium Ion Battery. *Electrochim. Acta* **2016**, *191*, 385–391. <https://doi.org/https://doi.org/10.1016/j.electacta.2016.01.105>.
- (63) Beda, A.; Villevieille, C.; Taberna, P.-L.; Simon, P.; Matei Ghimbeu, C. Self-Supported Binder-Free Hard Carbon Electrodes for Sodium-Ion Batteries: Insights into Their Sodium Storage Mechanisms. *J. Mater. Chem. A* **2020**, *8* (11), 5558–5571. <https://doi.org/10.1039/C9TA13189B>.
- (64) Beda, A.; Vaultot, C.; Matei Ghimbeu, C. Hard Carbon Porosity Revealed by the Adsorption of Multiple Gas Probe Molecules (N₂, Ar, CO₂, O₂ and H₂). *J. Mater.*

- Chem. A* **2021**, *9* (2), 937–943. <https://doi.org/10.1039/D0TA10088A>.
- (65) Qiu, S.; Xiao, L.; Sushko, M. L.; Han, K. S.; Shao, Y.; Yan, M.; Liang, X.; Mai, L.; Feng, J.; Cao, Y.; Ai, X.; Yang, H.; Liu, J. Manipulating Adsorption–Insertion Mechanisms in Nanostructured Carbon Materials for High-Efficiency Sodium Ion Storage. *Adv. Energy Mater.* **2017**, *7* (17), 1700403. <https://doi.org/https://doi.org/10.1002/aenm.201700403>.
- (66) Memarzadeh Lotfabad, E.; Kalisvaart, P.; Kohandehghan, A.; Karpuzov, D.; Mitlin, D. Origin of Non-SEI Related Coulombic Efficiency Loss in Carbons Tested against Na and Li. *J. Mater. Chem. A* **2014**, *2* (46), 19685–19695. <https://doi.org/10.1039/C4TA04995K>.
- (67) Cao, Y.; Xiao, L.; Sushko, M. L.; Wang, W.; Schwenzler, B.; Xiao, J.; Nie, Z.; Saraf, L. V.; Yang, Z.; Liu, J. Sodium Ion Insertion in Hollow Carbon Nanowires for Battery Applications. *Nano Lett.* **2012**, *12* (7), 3783–3787. <https://doi.org/10.1021/nl3016957>.
- (68) Meng, Q.; Lu, Y.; Ding, F.; Zhang, Q.; Chen, L.; Hu, Y.-S. Tuning the Closed Pore Structure of Hard Carbons with the Highest Na Storage Capacity. *ACS Energy Lett.* **2019**, *4* (11), 2608–2612. <https://doi.org/10.1021/acseenergylett.9b01900>.
- (69) Zhang, X.; Dong, X.; Qiu, X.; Cao, Y.; Wang, C.; Wang, Y.; Xia, Y. Extended Low-Voltage Plateau Capacity of Hard Carbon Spheres Anode for Sodium Ion Batteries. *J. Power Sources* **2020**, *476*, 228550. <https://doi.org/https://doi.org/10.1016/j.jpowsour.2020.228550>.
- (70) Suo, L.; Zhu, J.; Shen, X.; Wang, Y.; Han, X.; Chen, Z.; Li, Y.; Liu, Y.; Wang, D.; Ma, Y. Hard Carbon Spheres Interconnected by Carbon Nanotubes as High-Performance Anodes for Sodium-Ion Batteries. *Carbon N. Y.* **2019**, *151*, 1–9.

<https://doi.org/https://doi.org/10.1016/j.carbon.2019.05.030>.